Pergamon

Int. J. Solids Structures Vol. 32, No. 6/7, pp. 991–1002, 1995

0020-7683/95 $9.50 + .00

0020-7683(94)00173-1

THREE-DIMENSIONAL EFFECTS ON STRESS INTENSITY FACTOR DISTRIBUTIONS AND CRACK GROWTH IN MOTOR GRAIN MODELS

C. T. LIU
Phillips Laboratory, Edwards AFB, CA 93524-7160, U.S.A.

and

C. W. SMITH and L. WANG
Department of Engineering Science and Mechanics, Virginia Polytechnic Institute and State University, Blacksburg, VA 24061-0219, U.S.A.

(*Received* 15 *December* 1993; *in revised form* 12 *May* 1994)

Abstract—This paper reviews the results of a frozen stress photoelastic study of the growth and stress intensity factor distributions for surface flaws emanating from the tip of a fin in motor grain models along and off the axis of symmetry of the fin. The cracks were grown under monotomically increasing internal pressure above the critical temperature of the model material. For the non-symmetric cracks, a two-dimensional finite element model was found to closely predict the crack midpoint path (along principal planes of stress). Crack shapes and stress intensity factor (SIF) distributions, together with a simple, predictive model for symmetric cracks are included.

INTRODUCTION

An important engineering problem in structural design of solid rocket motors is the evaluation of structural integrity and reliability. It is known that the strength may be degraded by the presence of cracks in the material. In order to determine the severity of the crack or the ultimate service life of the structure, the failure criterion should include the crack propagation aspect of localized failure. Since the crack growth behavior is controlled by the local stress at the crack tip, the distribution of the stress intensity factor along the crack front needs to be determined.

The application of the frozen stress photoelastic method to the study of stresses in rocket motor grain is not new. An excellent discourse on this subject has been given by Durelli (1967). Subsequently, Francis *et al.* (1972) studied the pressurized crack behavior in two-dimensional models of motor grain shapes and Francis *et al.* (1974) also presented an analysis for viscoelastic cracking of simple shapes. Until recently, however, no experimental studies had been directed to the determination of stress intensity factor distributions along crack fronts in motor grain body shapes.

During the past years, the authors investigated the effects of crack size and location on the distribution of the mode I stress intensity factor along the crack front. The model material was a stress freezing epoxy which above its critical temperature becomes soft and rubbery. It accurately represents boundary effects for an elastic continuum which is a reasonable model of solid propellant of near the low mil-spec temperatures of $-60°F$ where cracking is a problem. In the present paper the results of these studies will be summarized.

TEST PROCEDURES

The frozen stress method was employed in the present study. Photoelastic motor grain models were cast and surface flaws in radial planes were introduced in the following way (refer to Fig. 1).

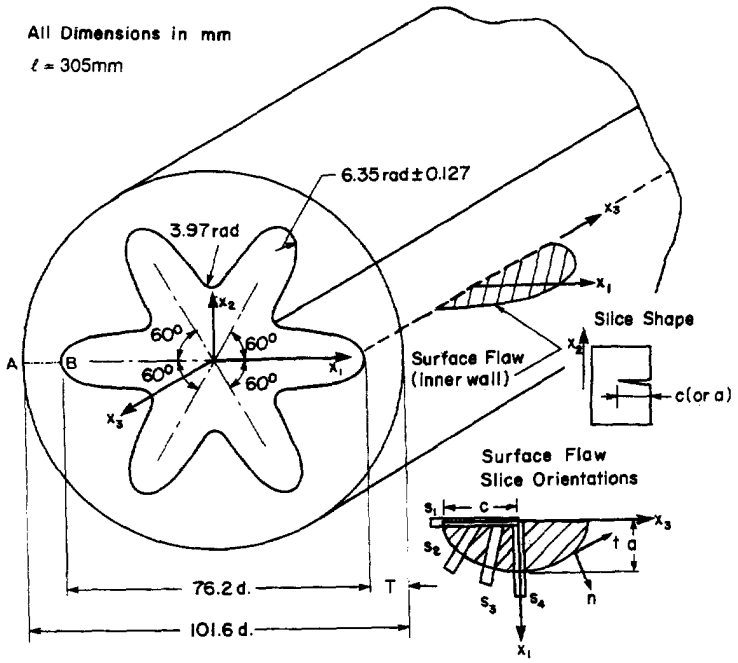

Fig. 1. Test specimen and slice orientation.

(i) Drill a hole through the wall of the model diametrically opposite to the star finger to be cracked.
(ii) Slide a shaft with a sharp blade mounted on its end through the hole and position the blade for a radial cut.
(iii) Strike the blade with a hammer. A natural crack then emanates from the blade tip and forms a starter surface flaw.
(iv) The hole is then plugged with a disk of the model material and glued in.
(v) After heating to critical temperature, sufficient pressure is applied to grow the crack to the approximate desired size while viewed through a glass oven port.
(vi) Pressure is then reduced to stop crack growth and the model is cooled and sliced according to Fig. 1.

DATA ANALYSIS

When a frozen stress experiment is conducted on a cracked body, thin slices are removed mutually orthogonal to the crack surface and the crack border for analysis in a polariscope for the local fringe pattern. Since the photoelastic effect averages data through the thickness, it is desirable to cut the slice as thin as possible to minimize averaging along the flaw border. Moreover, since stress freezing material is quite soft above the critical temperature, loads must be kept small to avoid finite deformation in the measurement zone. Since both of these considerations result in a significant reduction in the number of stress fringes available, it is necessary to modify the standard polariscope so as to optically increase the number of fringes occurring near the crack tip. This may be accomplished by the tandem application of the Tardy method (1929) for fractional fringe order analysis and the Post method (1966) for fringe multiplication. A test set-up for this procedure is shown in Fig. 2 which was constructed by Smith and Epstein (1984). A typical mode I multiplied fringe pattern is shown in Fig. 3. Since all of the studies involved growing cracks, only a mode I algorithm was needed to convert the photoelastic data into stress intensity factor values. This algorithm is briefly described in the following paragraphs.

In linear elastic fracture mechanics (LEFM) using the photoelastic approach, one can begin with mode I near-tip equations (Fig. 4)

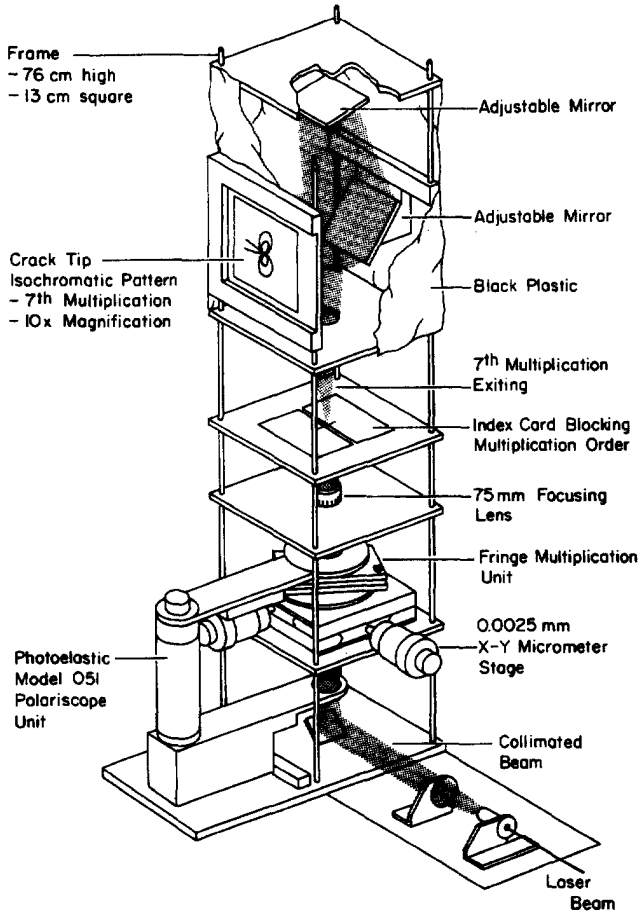

Fig. 2. Refined polariscope.

$$\sigma_{ij} = \frac{K_I}{\sqrt{8\pi r}} f_{ij}(\theta) + \sigma_{ij}^0 \quad (i, j = n, z) \tag{1}$$

where K_I is the mode I SIF, σ_{ij}^0 are the contributions of the nonsingular stresses in the measurement zone, and r, θ then are centered at the crack tip. The following expression is computed, in truncated form, along $\theta = \pi/2$.

$$\tau_{\max}^{nz} = \frac{K_{Ap}}{\sqrt{8\pi r}} = \frac{K_I}{\sqrt{8\pi r}} + \tau_0 \tag{2}$$

where K_{Ap} is an "apparent" SIF which includes the effects of σ_{ij}^0 {i.e. $\tau_0 = f(\sigma_{ij}^0)$} with the singular effect in the measurement zone. By rearranging terms in eqn (2) and normalizing, we can obtain

$$\frac{K_{Ap}\Phi}{p\sqrt{\pi a}} = \frac{K_I\Phi}{p\sqrt{\pi a}} + \frac{\sqrt{8}}{p}\tau_0\Phi\left(\sqrt{\frac{r}{a}}\right) \tag{3}$$

where the coefficient of $\sqrt{r/a}$ is a constant, p is the internal pressure and a is the crack size. Φ is an elliptic integral which varies with the aspect ratio of the crack (a/c). Its form is given in Fig. 5.

Equation (3) suggests that the normalized K_{Ap} varies linearly with the square root of the normalized distance from the crack tip $\{\sqrt{r/a}\}$ in the singularity dominated zone. Thus, by plotting the digitized raw data, $[K_{Ap}\Phi/p\sqrt{\pi a}]$ versus $[\sqrt{r/a}]$, the linear zone may be

found. Then, using a least squares fit, the line representing these data can be constructed and extrapolated across a near-tip nonlinear zone to determine the normalized K_I [i.e. $K_I\Phi/p\sqrt{\pi a}$] at the crack tip. The linear zone is normally just outside $\sqrt{r/a} \approx 0.2$, but should be at the same location for all slices on the same crack. Figure 5 illustrates this process for an interior slice from the flaw border.

RESULTS AND DISCUSSION

The geometric parameters of cracks which are symmetrically located with respect to the plane of the fin are given together with the corresponding SIF distributions in Fig. 6. From Fig. 6 one may conclude that, except for the shallow flaws, there is only negligible variation of the SIF around the flaw border. The same result was found from a finite element analysis (Raju and Newman, 1982) of a surface flaw in a pressurized cylinder. Using that analysis and the experimental data, one can compute a fictitious inner radius such that the two sets of results agree. This suggests that, except for shallow cracks, the geometry of the star shaped cutout has little effect upon the SIF distribution. Moreover, it is likely that two-dimensional finite element models may adequately predict SIF values for symmetrically cracked cylinders with star shaped cutouts under internal pressure. This would be expected to hold for deep cracks but not necessarily for very shallow cracks. It was also observed that, in some cases, the orientation of the starter crack was at a slight angle to the star fin axis of symmetry. This led to the presence of a very small shear mode at the starter crack tip when pressurized. However, as the crack was grown under pressure, it quickly returned to the plane of symmetry of the fin.

In determining the SIF near the inner star surface, an LEFM algorithm was used and so the order of the stress singularity was assumed to be one half. Although some difference in the SIF values from test replications here was noted, they are believed to be due to experimental scatter in extracting data from variable thickness slices and not due to the vertex singularity effect.

Since little variation of the SIF distribution around the flaw border occurred, except for the shallow flaws, and even here the maximum SIF occurred at maximum depth, it would seem efficient to employ a two-dimensional model for predicting the SIF at maximum flaw penetration for use in analysis and design. As a first attempt, the authors propose the following equation where K_{wt} is constructed from displacements (u_y) and SIF (K_j) obtained by Jones (1974) for a diametrically compressed cylinder containing a radial straight front crack emanating from the inner surface in the plane of the loads:

$$K_I = f(a)\, K_{wt} \left[\frac{K_{NR}}{K_{BF}}\right] \tag{4}$$

where $(x, y) \rightarrow (n, z)$ at maximum flaw penetration for K_{wt}

K_I = SIF at maximum flaw penetration

$K_{wt} = f(a) p(x)\, m(x, a)\, dx$

$p(x)$ = $\sigma_{\theta\theta}$ along the axis of symmetry determined from the isochromatic pattern of the uncracked model

$$m(x, a) = \frac{E}{2(1-\nu^2)\, K_I} \frac{\partial u_y(x, a)}{\partial a}$$

K_j = SIF from the Jones solution (Jones, 1974)

K_{BF} = SIF from the Bowie–Freese solution (Bowie and Freese, 1972) for a radial straight front crack in a pressurized cylinder

E, ν = elastic constants

u_y = crack opening displacements from Jones (1974)

a = crack depth

$f(a)$ = $1.19 + 0.90a - 6.62a^2$, a polynomial correction factor to account for use of

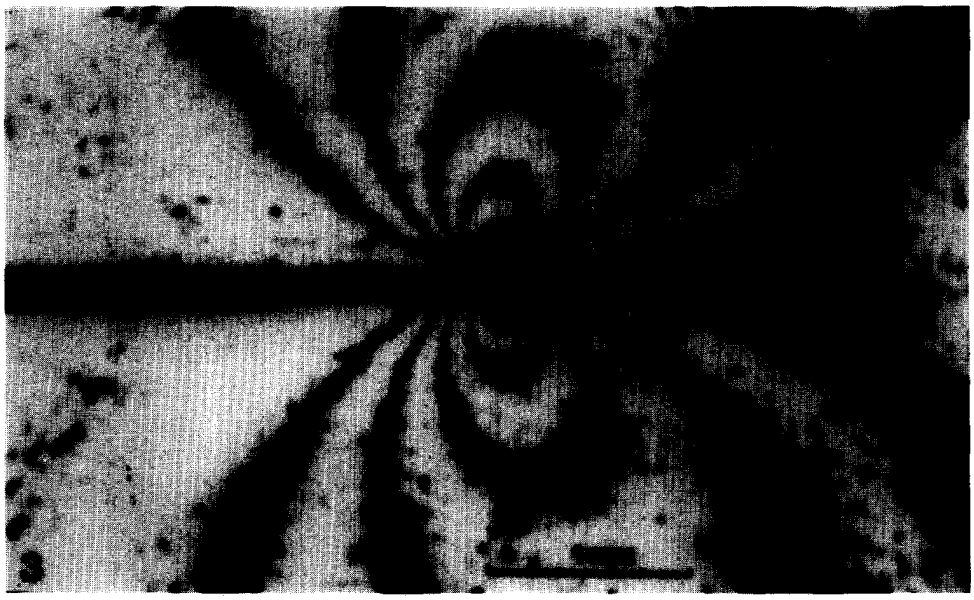

Fig. 3. Center slice (S_4 in Fig. 1), 9th multiple slice thickness 0.35 mm.

Fig. 13. Stress fringe pattern for uncracked body.

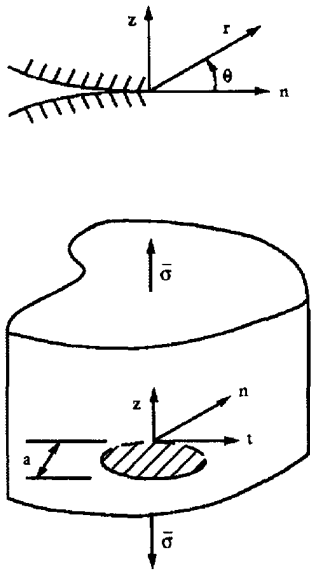

Fig. 4. Crack geometry and notation.

$m(x, a)$ due to a through crack† in a cylinder

K_{NR} = Newman–Raju solution (Raju and Newman, 1982) for SIF at maximum flaw depth.

The geometric parameters of cracks which are nonsymmetrically located with respect to the plane of the fin are given in Table 2.

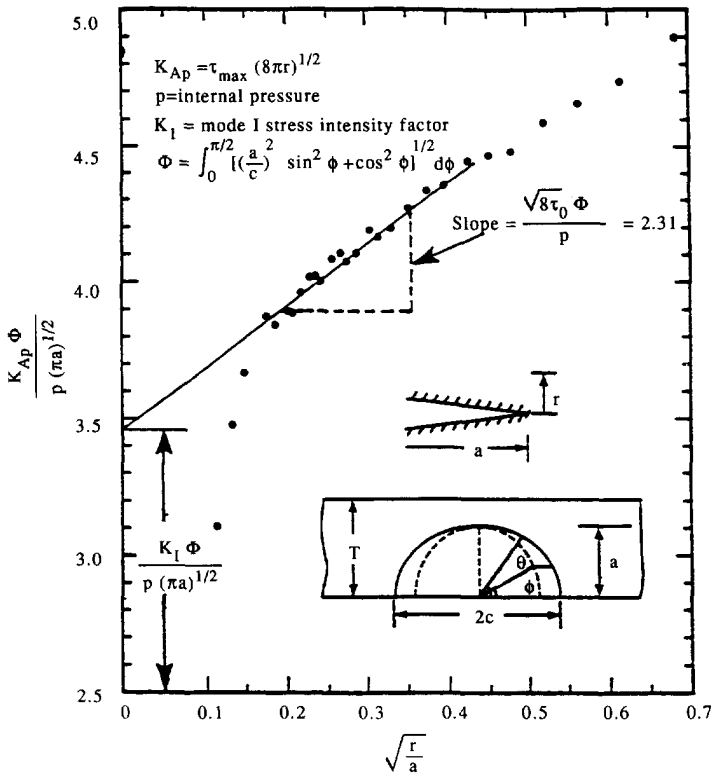

Fig. 5. Determination of SIF from slice data.

†This form of $f(a) = K_I K_{BF}/K_{w_1} K_{NR}$ yields the correlation coefficient of 0.98.

Table 1. Data for symmetric cracks

Test no.	a (mm)	a/c	a/T	Φ†	p (KPa)‡
T0	3.6	0.54	0.28	1.23	26.9
T1	3.2	0.52	0.25	1.22	47.6
T2	4.1	0.55	0.32	1.24	47.6
T3	6.2	0.46	0.45	1.18	47.6
T4	6.6	0.52	0.52	1.22	42.1
T5	7.3	0.43	0.56	1.16	47.6
T6	8.4	0.44	0.66	1.17	47.6
T7	7.9	0.45	0.62	1.17	47.6

† See Fig. 5.
‡ Internal pressure.

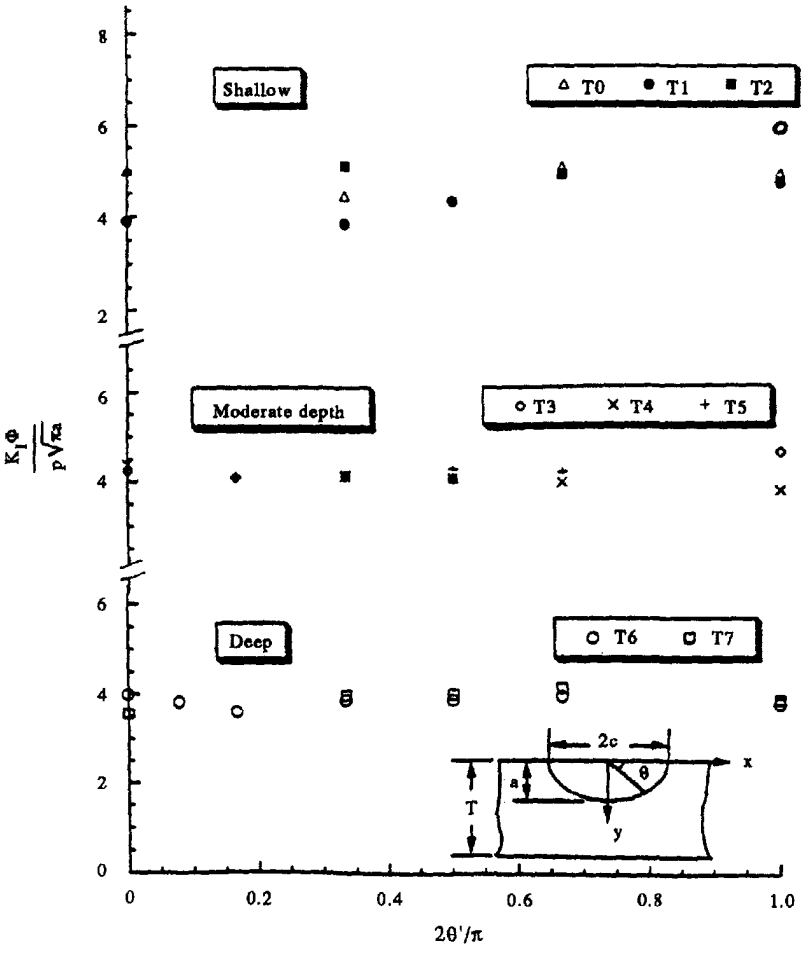

Fig. 6. SIF distributions around surface flaws.

Table 2. Geometric parameters of the off-axis cracks

Test I.D.	a'(mm)	c (mm)	T' (mm)	a'/T'	a'/c
E1	11.4	18.5	13.0	0.88	0.62
E2	13.2	19.1	13.2	1.0	0.69
E3	7.87	12.4	13.0	0.61	0.63
E4	11.2	14.0	13.7	0.82	0.80
E5	13.9	11.3	13.9	1.0	1.23

$B = 30°$ for E1, E2, E3, $a_0 \approx 1.25$ mm; $B = 45°$ for E4, E5, $a_0 \approx 2.25$ mm.

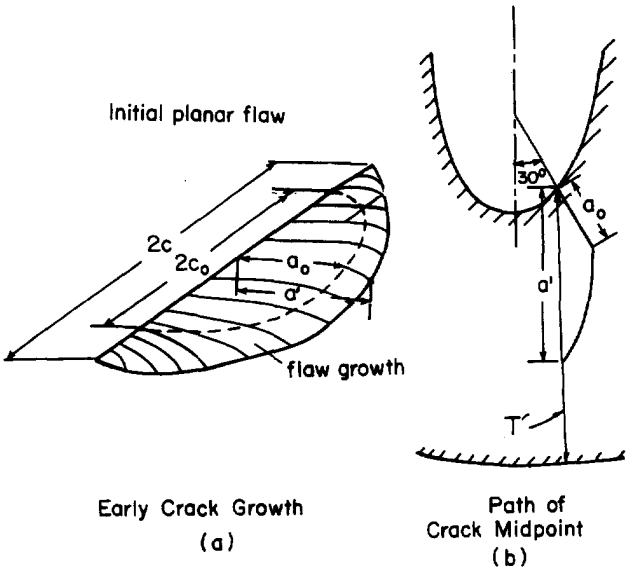

Fig. 7. Off-axis crack shapes and definitions of geometric parameters ($2c_0$, a_0—plane starter crack dimensions; a'—projected final crack depth).

Experimental evidence revealed that the initially semi-elliptic cracks grew into non-planar cracks and they were approximately symmetrical with respect to the crack midpoint path. A schematic representation of the growing of the unsymmetric crack is shown in Fig. 7. In Fig. 7, the sharp change in direction from a_0 is required to find the plane of maximum tension and eliminate any shear modes present in the starter crack orientation. Since the starter cracks were semi-elliptic, the quantity a' was used to compute Φ' values for a pseudo-semi-elliptic shape.

Figure 8 shows the midpoint crack paths. Two of the cracks, E2 and E5, penetrated the outer surface of the model and revealed a point of inflection in the crack path suggesting that, beyond a certain depth, the crack's path is dominated by the outer surface. All of the $\beta = 30°$ cracks exhibited about the same aspect ratio and the corresponding SIF distributions are shown in Fig. 9 which were obtained by using the algorithm described earlier. Comparing E1 and E3, it appears that the proximity of the outer surface elevates the SIF distribution along the part of the crack near the outer surface. Then, when the crack E2 breaks through to the outer surface, the SIF level is elevated along the uncracked portion of the crack.

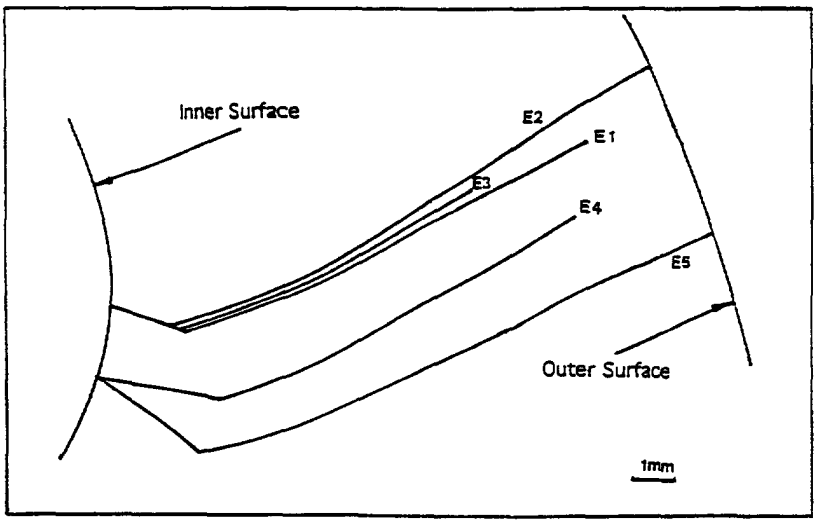

Fig. 8. Propagation paths of midpoints of off-axis cracks.

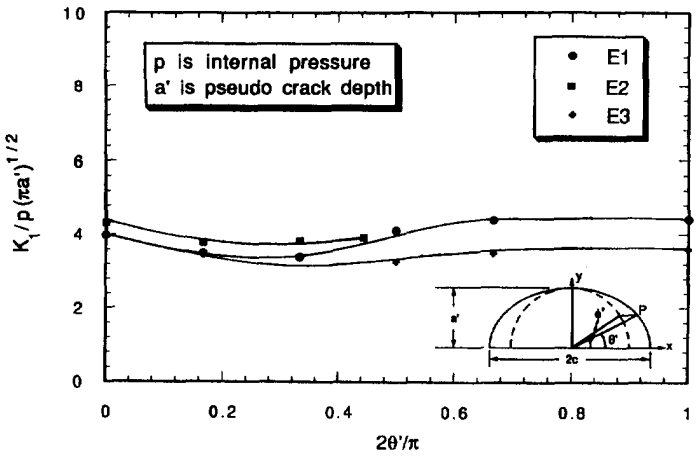

Fig. 9. Normalized SIF distributions for 30° off-axis cracks.

On the other hand, the $\beta = 45°$ cracks revealed a different behavior (Fig. 10) in that the penetrated crack indicates a lower SIF distribution along its remaining tip than the crack tip prior to penetration. This is believed due to the drastic difference in aspect ratios (a'/c) between the two cracks due to their different locations. If we compare the projected penetrated geometries of E2 and E5 (Fig. 11), it appears that the shape of E2 is beginning to approximate a straight through crack, while E5 still has a predominantly "part through" crack shape. This might explain the elevation in the SIF distribution in E2 not present in E5.

It has been postulated (Cotterell, 1965, 1966; Cotterell and Rice, 1980) that growing cracks follow planes of maximum principal tensile stress. Figure 12 shows a comparison between the crack path predicted by a photoelastic analysis of the uncracked body (Fig. 13) with the actual midpoint crack path and a two-dimensional finite element model. Differences in path which accrue with increasing crack depth may well be due to the relatively large band widths of the isoclinics.

CONCLUSIONS

A three year study focusing on an attempt to experimentally evaluate the effects of crack size and location on the stress intensity factor distribution along the crack front was reviewed. The main findings are as follows:

(i) The aspect ratio changed as the crack grew deeper.

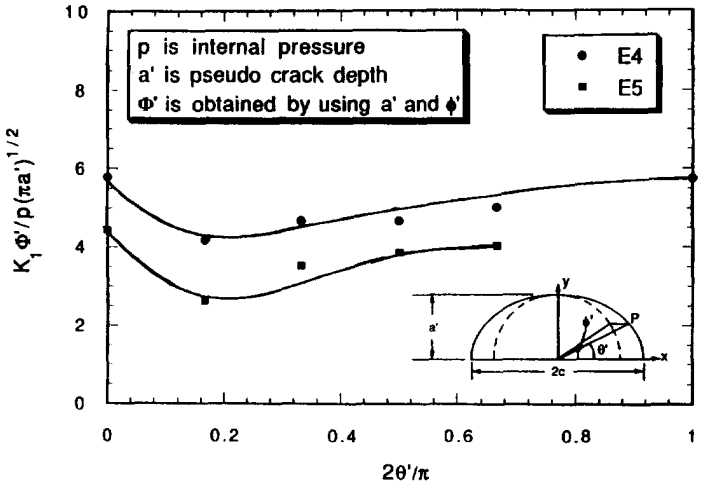

Fig. 10. Normalized SIF distributions for 45° off-axis cracks.

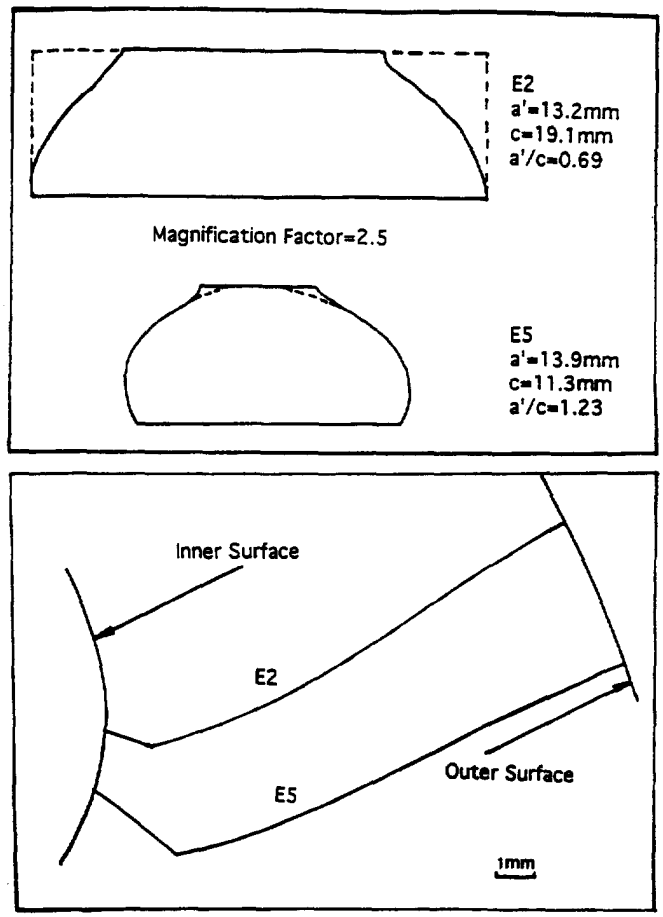

Fig. 11. Crack shapes for penetrated cracks.

(ii) For symmetrically located cracks, the SIF distribution along the crack front was essentially uniform and the crack plane was a principal plane of stress.
(iii) Only mode I stress fringe signatures were observed for growing cracks.
(iv) The path of the midpoint of each nonsymmetric crack tended to approach the direction of the surface of maximum principal tensile stress in the uncracked model.

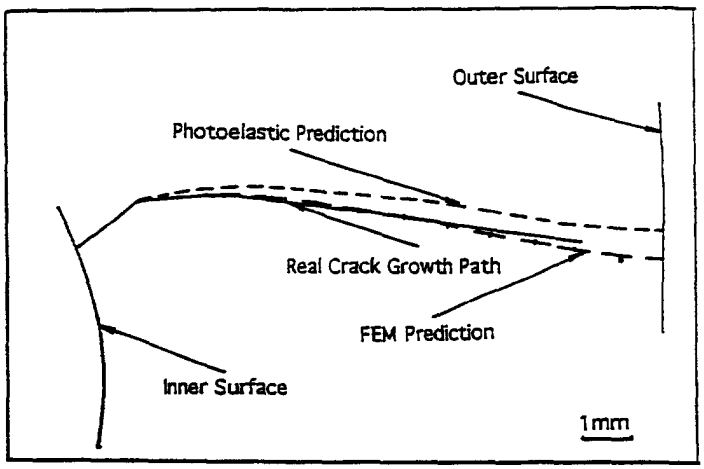

Fig. 12. Comparison of 30° off-axis crack midpoint path with photoelastic predictions of principal plane locations.

(v) There appeared to be a tendency for the crack shapes to develop approximately symmetrically with respect to the crack midpoint path.

(vi) SIF distributions along crack midpoint paths were non-uniform in the non-symmetrically located cracks and tended to be a maximum at the fin surface for penetrated flaws and at either the fin surface or maximum flaw depth for non-penetrating flaws.

The above observations are based upon very limited experimental results and, especially for the $\beta = 45°$ flaws, beg for additional experimental verification. However, it may be possible to use the approximately symmetrical response of off-axis cracks to advantage by studying midpoint crack paths as described here in complex three-dimensional problems.

Acknowledgements—The authors wish to acknowledge the support of Phillips Laboratory under Contract No. FO-4611-88-K with Virginia Polytechnic Institute and State University for support of the studies described above.

REFERENCES

Bowie, O. L. and Freese, C. E. (1972). Elastic analysis for a radial crack in a circular ring. *J. Engng Fract. Mech.* **4**, 315–321.

Cotterell, B. (1965). On brittle fracture paths. *Int. J. Fract.* **1**, 96–103.

Cotterell, B. (1966). Notes on paths and stability of cracks. *Int. J. Fract. Mech.* **2**, 526–533.

Cotterell, B. and Rice, J. R. (1980). Slightly curved or kinked cracks. *Int. J. Fract.* **16**, 155–169.

Durelli, A. J. (1967). Experimental strain and stress analysis of solid propellant rocket motors. In *Mech. Chem. Solid Propellants, Proc. 4th Symp. Naval Struct. Mech.*, pp. 381–442. Pergamon Press, Oxford.

Francis, E. C., Lindsay, G. H. and Parmeter, R. R. (1972). Pressurized crack behavior in two-dimensional rocket motor geometries. *J. Spacecraft* **9**(6), 415–419.

Francis, E. C., Carton, C. H. and Lindsay, G. H. (1974). Viscoelastic fracture of solid propellant in pressurization loading conditions. *J. Spacecraft* **11**(10), 691–696.

Jones, A. T. (1974). A radially cracked, cylindrical fracture toughness specimen. *Engng Fract. Mech.* **6**, 435–446.

Post, D. (1966). Fringe multiplication in three-dimensional photoelasticity. *J. Stain Anal.* **1**(5), 380–388.

Raju, I. S. and Newman, J. C., Jr (1982). Stress intensity factors for internal and external surface cracks in cylindrical vessels. *J. Pressure Vessel Tech.* **104**, 293–298.

Smith, C. W. and Epstein, J. S. (1984). Measurement of three-dimensional effects in cracked bodies. *Proc. 5th Int. Congress Expl Mech.*, pp. 102–110. Society for Experimental Stress Analysis.

Tardy, M. H. L. (1929). Méthode pratique déxamen de mesure de la birefringence des verres dóptique. *Optics Rev.* **8**, 69–69.